

Rydberg excitation of trapped cold ions: a detailed case study

This article has been downloaded from IOPscience. Please scroll down to see the full text article.

2011 New J. Phys. 13 075014

(<http://iopscience.iop.org/1367-2630/13/7/075014>)

View [the table of contents for this issue](#), or go to the [journal homepage](#) for more

Download details:

IP Address: 138.232.183.11

The article was downloaded on 27/03/2013 at 15:51

Please note that [terms and conditions apply](#).

Rydberg excitation of trapped cold ions: a detailed case study

F Schmidt-Kaler¹, T Feldker¹, D Kolbe², J Walz², M Müller³,
P Zoller³, W Li⁴ and I Lesanovsky^{4,5}

¹ Institut für Physik, Johannes Gutenberg-Universität Mainz, D-55099 Mainz, Germany

² Institut für Physik, Johannes Gutenberg-Universität Mainz and Helmholtz-Institut Mainz, D-55099 Mainz, Germany

³ Institute for Theoretical Physics, University of Innsbruck, and Institute for Quantum Optics and Quantum Information of the Austrian Academy of Sciences, Innsbruck, Austria

⁴ Midlands Ultracold Atom Research Centre (MUARC), School of Physics and Astronomy, The University of Nottingham, Nottingham NG7 2RD, UK
E-mail: igor.lesanovsky@nottingham.ac.uk

New Journal of Physics **13** (2011) 075014 (25pp)

Received 15 April 2011

Published 29 July 2011

Online at <http://www.njp.org/>

doi:10.1088/1367-2630/13/7/075014

Abstract. We present a detailed theoretical and conceptual study of a planned experiment to excite Rydberg states of ions trapped in a Paul trap. The ultimate goal is to exploit the strong state-dependent interactions between Rydberg ions to implement quantum information processing protocols and simulate the dynamics of strongly interacting spin systems. We highlight the promise of this approach when combining the high degree of control and readout of quantum states in trapped ion crystals with the novel and fast gate schemes based on interacting giant Rydberg atomic dipole moments. We discuss anticipated theoretical and experimental challenges on the way to its realization.

⁵ Author to whom any correspondence should be addressed.

Contents

1. Introduction	2
1.1. Overview	3
2. Ion trap	5
2.1. Experimental setting	5
3. Laser system	7
3.1. Principle of vacuum ultraviolet generation	7
3.2. Laser setup	9
3.3. Vacuum ultraviolet power estimate and linewidth	9
3.4. Ion laser cooling, excitation and detection of single Rydberg ions	10
4. Single ion theory	12
4.1. Rydberg ion in a linear Paul trap	12
4.2. Calculation of Rydberg energies and wave functions	14
4.3. Bare electronic level structure	15
4.4. Laser excitation of Rydberg states	15
4.5. Electron–trap interaction	16
4.6. Electron–ion coupling	18
4.7. Adiabatic potential surfaces	19
4.8. State-changing transitions in the nP_j -manifold	21
5. Conclusion and outlook	22
Acknowledgments	23
References	23

1. Introduction

Coherent Rydberg physics with ensembles of ultracold atoms is a flourishing and rapidly growing field that currently receives much attention across area boundaries. The reason for this interest is rooted in the remarkable properties of highly excited atoms, which offer a new approach for the study of strongly correlated many-body physics and the implementation of quantum information processing protocols [1]. Rydberg atoms, where the outer valence electron is excited to high-lying electronic states with large principal quantum number n , interact strongly via dipolar or van der Waals interactions, which can lead to interaction energies of several MHz over distances of several micrometers.

The hallmark and key mechanism underlying coherent Rydberg physics is the so-called dipole blockade. This blockade hinders two atoms from being simultaneously excited when localized within a certain blockade radius: the interaction between two nearby atoms is here so strong that the doubly excited state is shifted out of the laser resonance [2–4]. In dense gases this drastically influences the excitation behavior when atoms are photo-excited to Rydberg states. This effect has been experimentally demonstrated both in dense atomic ensembles [5, 6] and for two atoms stored in nearby optical dipole traps [7, 8], where the latter setup has enabled the first realization of entangling two-qubit gate operations for neutral atoms [9, 10]. This remarkable experimental progress has stimulated a number of theoretical works: these include the exploration of novel quantum phases [11, 12], the study of the coherent real-time dynamics of strongly driven Rydberg gases [13–15], the development of new schemes for the efficient

generation of entanglement [16–20] and the development of a quantum simulation architecture for open-system dynamics of complex many-body spin models [21], based on Rydberg atoms stored in optical lattices [22] or magnetic trap arrays [23].

In a recent work [24], some of the present authors suggested the use of Rydberg excitations in ion traps to simulate many-body spin systems and to implement quantum information processing protocols. At present, laser-cooled and trapped ion crystals [25] provide one of the most precisely controllable many-body quantum systems available in the laboratory [26, 27]. Ions can be addressed individually by laser light performing operations on the internal electronic structure representing a spin or qubit [28]. The last decade has seen various experimental realizations of entangling quantum gates with a fidelity better than 99% [29], the demonstration of simple quantum algorithms, entanglement swapping, teleportation [30, 31] and recently the generation of entanglement with up to 14 ions [32]. Moreover, over the last few years, the potential power of this ion trap quantum computer to emulate the physics of interacting many-body quantum spin-models [33] has been demonstrated in a series of remarkable recent experiments [34, 35]. Also, by combining coherent quantum gates and optical pumping as a dissipative element, the building blocks of an open-system simulator with trapped ions [36] have been realized in the laboratory [37].

The present experiments follow the paradigm of entangling qubits represented by internal electronic or spin degrees of freedom of trapped ions in a linear chain via common vibrational modes of the trapped ions representing a phonon data bus [38, 39]. For a linear (one-dimensional (1D)) ion trap, the mode spectrum for large crystal sizes becomes increasingly complex, and scalability of ion trap quantum computers is achieved by shuttling ions around [40–42] and by going to 2D trap arrays [43, 44]. In contrast, gates based on Rydberg interactions do not rely on common vibrational modes, and thus the ionic Rydberg gate may provide an interesting alternative approach to scalability. Additionally, Rydberg physics promises long-range and strong interactions, such that the interaction dynamics takes place on a nanosecond time scale, which is much faster than the external motion of the ion string. In [24], this idea was explored for the first time in some detail, and in particular, also the dynamics of a single Rydberg ion in the presence of the electric trapping fields was described as a composite object consisting of a highly excited valence electron and a core formed by the nucleus and closed inner electronic shells. In the parameter regime of interest the electronic wave function extends over distances larger than the localization length of the ionic core, but is still considerably smaller than the inter-ionic distances of a few micrometers. Also it was proposed to enhance and tune the interaction strength of ions in Rydberg states by employing microwave dressing techniques [24]. In the context of quantum simulation of many-body spin models, it was argued that the resulting interionic interactions would allow one to realize spin chain dynamics with coherent excitation transfer on a nanosecond time scale. Likewise, these state-dependent long-range interactions might be explored for realizing fast two-qubit quantum gates, potentially several orders of magnitude faster than used entangling operations via the common vibrational modes. Thus the ability to excite and manipulate Rydberg excitations of trapped ions could provide a new interesting route for implementing quantum information processing protocols and the study of many-body physics in ion traps.

1.1. Overview

The purpose of this work is to conduct a quantitative case study of the feasibility of performing coherent excitation of Rydberg states in a crystal of $^{40}\text{Ca}^+$ ions held in a Paul trap. Ultimately,

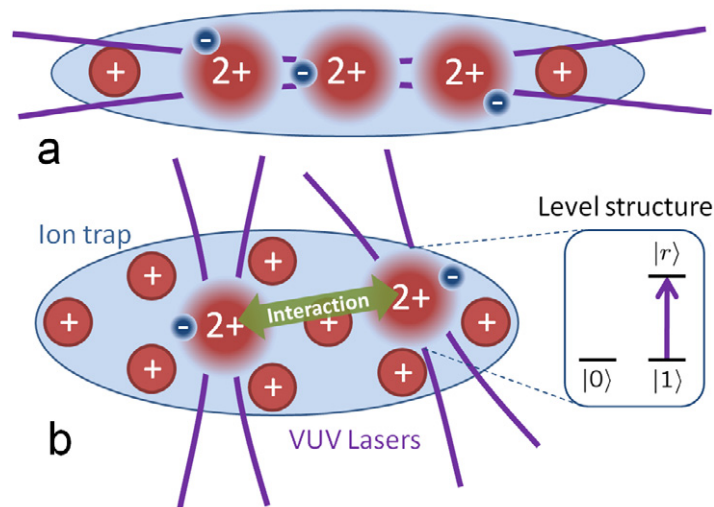


Figure 1. Envisioned setup. Cold $^{40}\text{Ca}^+$ ions confined in a Paul trap form a linear (a) or 3D (b) crystal. Each ion may encode a qubit in which the logical states $|0\rangle$ and $|1\rangle$ are stored in the ground state $3S_{1/2}$ and the long-lived $3D_{5/2}$ state, respectively. Two- or multi-qubit gate operations are realized by exciting a Rydberg state $|r\rangle$ of selected ions. Once excited, these ions interact over long distances and on a fast time scale, independently of the vibrational mode structure. The coherent excitation to the Rydberg state is achieved by a single vacuum ultraviolet (VUV) photon provided by tightly focused lasers.

this will lead to the creation of the coherent state-dependent interaction of an ion crystal as sketched in figure 1. We approach this task from three angles:

- (i) In section 2, we discuss in detail the envisioned *ion trap setup*. To demonstrate the coherent excitation of single ions to Rydberg states, we wish to create a trap with many ions configured in a linear string at the center of the trap or optionally an elongated 3D crystal. Here, the trapping of many ions will enhance the probability of exciting ions and simplify the task of aligning the narrow focus of the vacuum ultraviolet (VUV) laser to the ions. For the experimental study of Rydberg interactions at a later stage, this trap will be operated by trapping a few ions in a string configuration with small distances between the individual ions. We show that it is possible to reach both settings with a standard linear Paul trap that provides free access for all laser beams and the observation of the ion fluorescence. Furthermore, we explain the detection of single Rydberg excitations using an electron shelving scheme.
- (ii) Section 3 is dedicated to a detailed discussion of the *laser setup* that will be used to coherently excite ionic Rydberg states. In our envisioned scheme, Rydberg nP -states are excited from the metastable $3D_{5/2}$ state. One of the key challenges here is the required short wavelength close to 123 nm. This energy gap can, in principle, be overcome by using multi-photon excitation schemes [45]. We propose a different approach where the coherent excitation of Rydberg states is achieved by a single photon. We provide a study of how such a laser source is realized and how it is integrated into the ion trap setup. The key tool for such a continuous-wave (cw) VUV laser beam is four-wave mixing (FWM) in

mercury vapor with fundamental laser powers of several hundreds of mW. This is already an established technique for production of a coherent Lyman- α beam tuned to the 1S–2P transition in hydrogen at 121.56 nm [46, 47]. By choosing fundamental wavelengths close to resonances of mercury, the FWM efficiency can be strongly enhanced. A laser source around 123 nm with a power of a few μ W should be feasible by using a triple resonant FWM scheme [48].

- (iii) In the theory part of this paper (section 4), we provide a thorough theoretical analysis of the *quantum dynamics of a single trapped $^{40}\text{Ca}^+$ ion* that is excited to a Rydberg n P-manifold. We calculate the electronic energies and estimate the Rabi frequency for the laser excitation of Rydberg states. Our investigation reveals that the inhomogeneous field forming the Paul trap effectuates an inevitable coupling between the internal and external degrees of freedom of the ion. We calculate trapping field-induced electronic level shifts as a function of the principal quantum number and quantify the expected change of the trapping potential for Rydberg states. Furthermore, we analyze transitions among states within the n P-manifold that are induced by the oscillating trapping field. Our results show that the likelihood of such transitions strongly depends on the principal quantum number and on the phase of the radio-frequency (RF) field of the Paul trap.

2. Ion trap

In this section, we discuss the setup of the ion trap, which is designed for two categories of experiments with Rydberg ions. In the first step, we will investigate single ion excitation physics of $^{40}\text{Ca}^+$ to Rydberg states in the time-dependent potential of the ion trap. The adaptation of spectroscopic methods for the Rydberg states, the measurement of the line width of the excitation resonance and the selection of the optimal Rydberg level for further experiments are specific goals here, as well as the detection of wave packet dynamics in the dynamic potential of the ion trap which is theoretically investigated in section 4. Specifically suited for these experiments is a long string consisting of many ions as shown in figure 1(a) or even an elongated 3D ion crystal loaded into the trap. This geometry in conjunction with a proper alignment of the laser will allow us to increase the overall probability of exciting Rydberg ions.

The next step will be to study interaction effects between two ions when excited to Rydberg states. For these experiments we require ideally an inter-ion distance below the Rydberg blockade radius [3], which is accomplished by increasing the trap frequencies. In order to get similar Rabi frequencies for all ions, the ions should be configured in a linear string of a total length that is much shorter than the Rayleigh length of the focused VUV laser. The design of the trap allows us to reach both settings with the same trap geometry.

2.1. Experimental setting

We will trap $^{40}\text{Ca}^+$ ions in a linear Paul trap consisting of four cylindrical rods and two endcaps. The trap is shown together with the VUV laser setup in figure 2. The diameter of the rods is 2.5 mm, while the distance r_0 from the trap center to the rods is 1.1 mm. This ratio between the diameter and r_0 was chosen to optimize the quadrupole approximation for the electric field of the trap [49], thus enabling us to store 3D elongated crystals. The distance between endcaps of the trap is 10 mm. Calculations [50] yield, for an RF amplitude of $U_{\text{ac}} = 500$ V at a frequency of $\Omega = 2\pi \times 15$ MHz, a stability parameter of $q \approx 0.2$ and a radial confinement ω_r of about

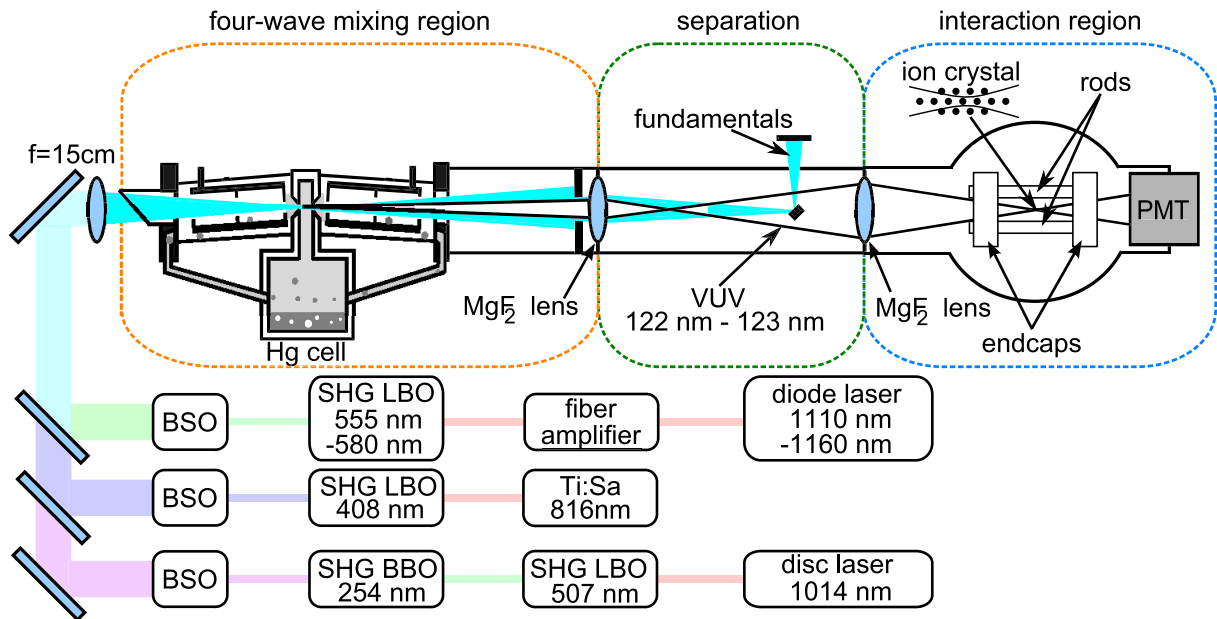


Figure 2. The VUV laser setup, beam guidance and excitation region. Lower part: schematic diagram of the fundamental laser systems (SHG, second harmonic generation; LBO and BBO, nonlinear crystals; BSO, beam shaping optics; Ti : Sa, titanium : sapphire laser). Upper part: the vacuum system. The overlapping fundamental beams are focused into the mercury cell where FWM takes place. Separation of the VUV beam from the fundamentals is achieved using the dispersion of a MgF_2 lens. A second MgF_2 lens both focuses the VUV beam into the ion crystal and seals the low vacuum region (at $\sim 10^{-4}$ Pa) from the ultrahigh vacuum (UHV) chamber (at $\sim 10^{-9}$ Pa) that contains the Paul trap. The VUV beam passes holes in the endcap electrodes of the trap and is monitored by a photomultiplier tube (PMT).

$2\pi \times 1$ MHz. To achieve an overlap of the beam with as many ions as possible, the VUV laser is aligned along the axis of the trap and propagates through holes in the endcaps. For the initial alignment of the VUV laser, we will aim at an elongated 3D crystal with a few concentric shells around the axis. Following [51], the density n_0 of the ions in such a crystal can be estimated as $(\epsilon_0 U_{ac}) / (M \Omega^2 r_0^4)$, where M is the mass of the ion. For the above trap parameters the distance between two ions is then approximately $11 \mu\text{m}$. Comparing this value to the waist of the VUV beam at the focus of only $1.5 \mu\text{m}$ and a Rayleigh length of $50 \mu\text{m}$, one finds that only the central string of ions will contribute to the Rydberg yield once the beam is properly aligned; hence, we will switch to a linear configuration of ions for the experiments with single Rydberg ions.

The maximum number N of trapped ions in a single linear string configuration depends on the ratio between the axial and radial trap frequencies [52]. The critical ratio is approximated by $(\omega_z / \omega_r)^2 = 2.94 \times N^{-1.8}$; hence, the linear string configuration is stable if the radial frequency is much higher than the axial one. Simulations of the axial trapping potential [53] result in ω_z of about $2\pi \times 80$ kHz for a dc voltage of $V_{dc} = 90$ V, which leads, together with the radial trap frequency of $2\pi \times 1$ MHz, to a linear string consisting of 30 ions with a total length of $250 \mu\text{m}$ [25]. Summing over the relative excitation probabilities of the individual ions I_z / I_0 ,

where I_z is the laser intensity at the place of the ion and I_0 the intensity in the focus, and assuming that the VUV beam is perfectly aligned with the ion string (see figure 1(a)), this setting allows us to increase the total probability of excitation to the Rydberg state by more than a factor of 15 as compared to spectroscopy with a single ion in the focus of the VUV beam. The detection scheme for the spectroscopy of Rydberg levels is outlined in section 3.4 and we point out that the use of a large linear ion crystal is helpful since the overall excitation probability is increased and the alignment of the laser beam at 123 nm with its very tight focus becomes less critical.

For later experiments investigating the dipole blockade between two Rydberg ions, the ions should be configured in a short linear chain on the trap axis. The distance between two ions has to be smaller than the blockade radius, which is estimated to be of the order of $5 \mu\text{m}$ [24]. The minimal distance between two ions depends on the axial confinement and the number of trapped ions and can be calculated [25] as

$$d_{\min} = \left(\frac{e^2}{4\pi\epsilon_0 M \omega_z^2} \right)^{1/3} \times \frac{2.081}{N^{0.559}}. \quad (1)$$

If we increase the parameters to an RF of $2\pi \times 30 \text{ MHz}$ with an amplitude of 2000 V and an endcap voltage of $U_{\text{dc}} = 1600 \text{ V}$, we get trapping frequencies of $\omega_r = 2\pi \times 2.2 \text{ MHz}$ and $\omega_z = 2\pi \times 400 \text{ kHz}$. This would lead to an ion crystal with $N = 12$ ions and a minimal inter-ion distance of $4.1 \mu\text{m}$. The different settings for the ion trap are illustrated in figure 3 showing (a) the increase in total excitation probability to the Rydberg state for different axial and radial trap frequencies and (b) the minimal distance between ions for experiments exploring the Rydberg blockade. For a further increase of the trap frequencies in order to get to distances of $3 \mu\text{m}$ and less, and in a later stage of the experiment, one might employ an advanced segmented micro trap [54].

3. Laser system

The light required for the Rydberg excitation from the $3D_{5/2}$ state to an nP_j state lies in the VUV region between 131 nm ($n = 10$) and 122 nm ($n \rightarrow \infty$). Four-wave mixing (FWM) is an established technique for producing cw light in this frequency regime [47, 55–57]. A good candidate as a nonlinear medium is mercury vapor, which provides suitable transitions enhancing the FWM efficiency. In this section, we will first discuss the principle of threefold one-photon resonant FWM that strongly enhances the mixing efficiency. In the second part the setup of the laser source will be presented and in the third part we estimate the laser power for different $3D_{5/2} \rightarrow nP_j$ transitions.

3.1. Principle of vacuum ultraviolet generation

Relevant levels of mercury and frequencies for the FWM process are shown in figure 4. The UV beam at 254 nm is red-detuned to the $6^1S \rightarrow 6^3P$ resonance. The blue beam at 408 nm establishes the two-photon resonance with the $6^1S \rightarrow 7^1S$ transition together with the UV beam. The third beam in the green wavelength region determines the output wavelength in the VUV due to FWM. The resulting power through FWM is given by [58]

$$P_4 = \frac{9}{4} \frac{\omega_1 \omega_2 \omega_3 \omega_4}{\pi^2 \epsilon_0^2 c^6} \frac{1}{b^2} \left(\frac{1}{\Delta k_a} \right)^2 |\chi_a^{(3)}|^2 P_1 P_2 P_3 G(b N_0 \Delta k_a). \quad (2)$$

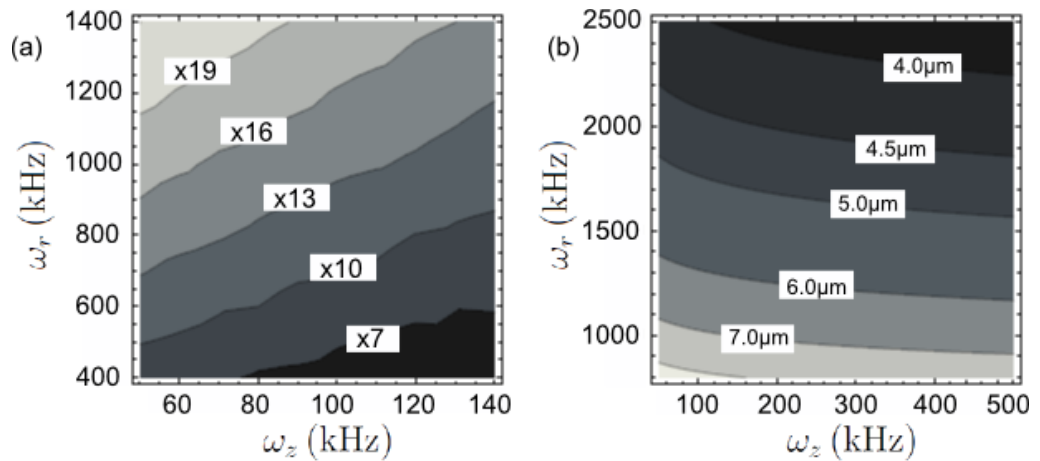


Figure 3. Dependence of the probability to excite a Rydberg ion on the trap settings. The left plot (a) shows the effective Rydberg excitation enhancement rate for a linear ion string compared to a single ion in the focus of the beam. Assuming that the trap is loaded with the maximum number of ions for a linear chain configuration, the excitation rate will increase for higher radial and lower axial trap frequencies. Within the given parameter region we can expect an enhancement by about a factor of 20. The right plot (b) shows the relationship between the trap frequencies and the minimal distance between two ions. Distances down to 4 μm are possible with realistic parameters for the voltages and RF frequency and the given trap geometry.

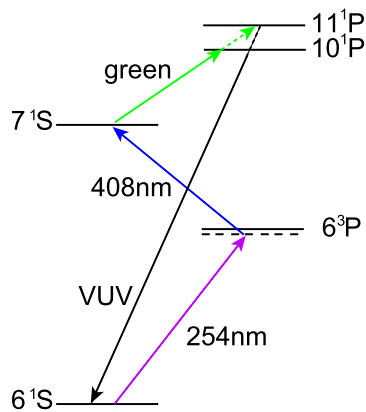


Figure 4. FWM in mercury vapor. The UV beam at 254 nm is close to the 6^1S – 6^3P resonance; the blue beam at 408 nm establishes together with the UV beam the two-photon resonance (6^1S – 7^1S). The green laser frequency determines the resulting wavelength of the four-wave mixed beam in the VUV.

Here ω_i is the angular frequency and P_i the power of the i th beam, N_0 the density of the nonlinear medium, $\chi_a^{(3)}$ the nonlinear susceptibility per atom and $\Delta k_a = (k_4 - k_1 - k_2 - k_3)/N_0$ the wavevector mismatch per atom. $G(bN_0\Delta k_a)$ is the phase-matching function for phase matching by the density of the nonlinear medium giving a maximum value at $bN_0\Delta k_a = -4$,

where b is the beam b -parameter given by twice the Rayleigh length. For efficient FWM the only free parameter, in addition to increasing the fundamental intensities by using higher powers and tighter focusing, is the nonlinear susceptibility per atom $\chi_a^{(3)}$. This can be enhanced by using fundamental wavelengths close to resonances of mercury. In particular, a two-photon resonance is essential for cw FWM [59]. Additionally, we use two one-photon resonances to further increase the FWM efficiency. Therefore, the UV wavelength is set close to the 6^1S – 6^3P resonance and the VUV wavelength is set close to the 10^1P and 11^1P resonance, respectively. This triple resonant scheme enhances the FWM up to 4 orders of magnitude and establishes a continuous VUV laser source in the μW power range [48].

3.2. Laser setup

A schematic diagram of the setup for VUV production is shown in figure 2. The three fundamental beams are shaped by pairs of spherical and cylindrical lenses. The beams are overlapping at dichroic mirrors and focused into the mercury cell using a fused silica lens with a focal length of 15 cm. The mercury cell can be heated to up to 240°C providing a mercury vapor density of up to $N_0 = 1.1 \times 10^{24} \text{ m}^{-3}$. Outside the focus region, cooled baffles are used to avoid condensation of mercury on the optics. The produced VUV light is separated from the fundamental light by dispersion at a MgF_2 lens ($f = 13 \text{ cm}$ at 123 nm and $f = 20 \text{ cm}$ at 254 nm) and a tiny mirror in the focus of the fundamental light. A second MgF_2 lens ($f = 12.5 \text{ cm}$ at 123 nm) separates the low vacuum region from the high vacuum region (trap) and focuses the VUV beam into the $^{40}\text{Ca}^+$ trap with a Rayleigh length of $50 \mu\text{m}$ and a beam waist of $1.5 \mu\text{m}$. The power in the VUV can be monitored by a photomultiplier behind the trap.

A schematic diagram of the fundamental laser system is shown in the lower part of figure 2. The beam at 254 nm is produced by a frequency-quadrupled Yb : YAG disc laser (ELS, VersaDisk 1030-50). Frequency-quadrupling is done with two resonant enhancement cavities, the first one using a lithium triborate crystal (LBO) as the nonlinear medium and the second one using a β -barium borate crystal (BBO). From 2 W of infrared (IR) light at 1015 nm, we obtain up to 200 mW of UV radiation. This system is, in principle, capable of producing up to 750 mW of UV light; for details see [60]. The second fundamental beam at 408 nm is produced by a frequency-doubled titanium : sapphire laser (Coherent, 899-21), pumped by a frequency-doubled Nd : YVO₄ laser (Coherent, V10). The external frequency-doubling cavity uses an LBO crystal. From 1.5 W of IR light at 816 nm, we obtain up to 500 mW of blue light.

For the desired VUV wavelength of 122–123 nm, the third fundamental beam must be in the wavelength region 555–580 nm. Frequency-doubling IR light produced by a Yb-fiber amplifier seems to be a feasible laser source for powers up to several watts in the green [61, 62]. A frequency-stabilized laser diode can be used as a seed laser. By splitting the amplification into two separated stages (a low power stage and a high power stage), we expect low amplified spontaneous emission and high damage threshold of the Yb-fiber. Frequency doubling in an external resonator with a noncritical phase-matched LBO as the nonlinear crystal should help achieve a conversion efficiency of more than 60%. Frequency tuning of the green beam can be done by tuning the oscillator frequency and matching the LBO temperature.

3.3. Vacuum ultraviolet power estimate and linewidth

For efficient FWM in the 123 nm region two resonances in mercury are relevant: 6^1S – 10^1P at 122.04 nm and 6^1S – 11^1P at 123.223 nm wavelength. Triplet states of mercury have several

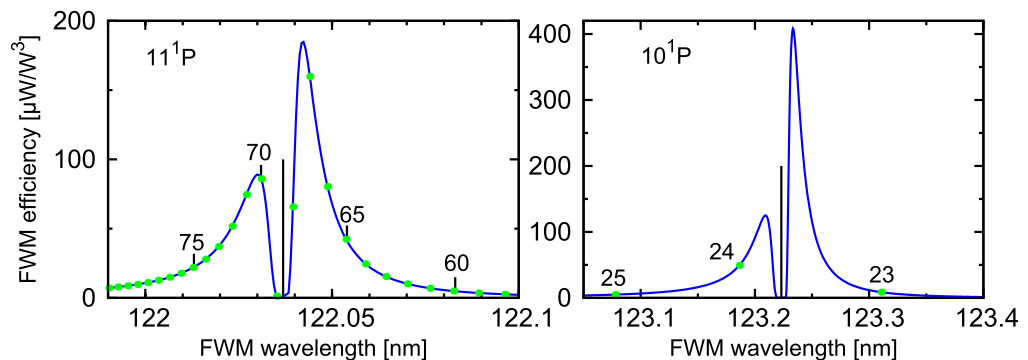


Figure 5. The FWM efficiency near the mercury resonances. Calculated efficiency of FWM close to the 11^1P (left) and 10^1P (right) states of mercury. The dots mark positions of $D_{5/2}-nP_{3/2}$ transition wavelength.

orders of magnitude smaller dipole moment to the ground state and therefore a much smaller influence on FWM. Figure 5 shows a calculation of the FWM efficiency near the two singlet states. On resonance, the VUV radiation generated is absorbed by the mercury vapor. In the proximity of a mercury resonance, however, the efficiency is much increased. The 10^1P state in mercury yields an efficiency of about $50 \mu\text{W W}^{-3}$ for the transition to the $24\text{P}_{3/2}$ state. And even an efficiency of $150 \mu\text{W W}^{-3}$ is achievable by using the 11^1P state of mercury, which corresponds to the $67\text{P}_{3/2}$ state of $^{40}\text{Ca}^+$. For the calculation, we took into account the absorption of VUV light in mercury vapor and imperfect fundamental beam qualities [63]. With moderate fundamental powers of 200 mW (UV), 300 mW (blue) and 3 W (green), we would obtain between $9 \mu\text{W}$ ($n = 24$) and $27 \mu\text{W}$ ($n = 67$). The corresponding Rabi frequencies are estimated in section 4.4. We expect saturation effects at several μW due to pumping of mercury out of the ground level, but a μW VUV source appears realistic with this setup.

The laser linewidth of the VUV source depends on the emission bandwidths of the three fundamental laser systems. In the present state, these laser systems are free-running. In an earlier experiment on Lyman- α excitation of atomic hydrogen [46], linewidths very close to the natural linewidth of the atomic transition have been observed. This gives an upper limit of 10 MHz laser linewidth at 121.6 nm. For the planned experiment, narrower linewidths are desired. We will thus frequency-stabilize the fundamental laser systems. A laser line width in the VUV in the MHz range and below seems feasible.

3.4. Ion laser cooling, excitation and detection of single Rydberg ions

In order to excite the ions to Rydberg states, they have to be prepared by Doppler cooling and subsequently optically pumped into the $3\text{D}_{5/2}$ state. The wavelengths of the required transitions for cooling and pumping are well suited for diode laser sources. Another advantage of the $^{40}\text{Ca}^+$ level structure is the very long lifetime of 1.2 s [64] of the intermediate $3\text{D}_{5/2}$ state, which is the lower state in the Rydberg excitation process. Figure 6 shows all relevant levels and transitions. To load the trap with ions, we will use photoionization, with diode lasers near 423 and 375 nm, or alternatively use multi-photon ionization with light at 532 nm from a pulsed Nd:YAG laser.

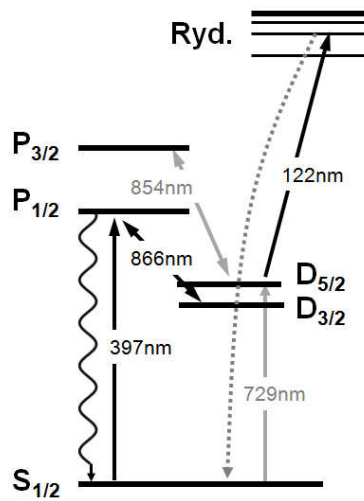


Figure 6. Excitation and detection scheme for $^{40}\text{Ca}^+$ ions. The ions are first pumped into the metastable $D_{5/2}$ state, from which they are excited to a Rydberg state by a pulse from the VUV laser. From the Rydberg state they will decay into the ground state. When the two lasers at 397 and 866 nm are switched on after the VUV pulse, the fluorescence of the ground state ion can be measured.

We propose a sequence of laser interactions, similar to standard ion trap quantum computing schemes, for the Rydberg excitation: first, the ions are (i) cooled on the $4S_{1/2}-4P_{1/2}$ transition near 397 nm close to the Doppler limit. Laser beams near 866 and 854 nm provide for optical pumping out of the metastable D-levels. The emitted fluorescence near 397 nm is imaged on the chip of an EMCCD camera. In a next step (ii), we optically pump all the ions into one of the Zeeman states of the $S_{1/2}$ ground state, switch off the laser at 854 nm and (iii) excite all ions in the crystal to the $3D_{5/2}$ level, which exhibits a 1.2 s lifetime. For the excitation we will rely on the efficient rapid adiabatic passage pulse [65]. In an initial stage of the experiment, one may incoherently optical pump into the desired metastable level via excitation to the $4P_{3/2}$ state at 393 nm, followed by decay to the $3D_{5/2}$ level by means of a UV light-emitting diode. Even when illuminated by resonant radiations near 397 and 866 nm, no fluorescence is emitted now. After the preparation of the ion crystal in the $3D_{5/2}$ level, all laser sources are switched off. The Rydberg state is then excited (iv) with a pulse of frequency ν_{Rydberg} near a wavelength of 123 nm. If an ion was excited successfully to the Rydberg state here, it will decay within a few tens to hundreds of μs [66], predominantly to the $4S_{1/2}$ ground state. Thus, after the excitation pulse, the laser beams at 397 and 866 nm may be switched on again (v) and the emitted fluorescence of the decayed ion can be detected with an EMCCD camera. Under typical operation conditions, we are able to discriminate between the on- and the off-state of fluorescence within 2 ms. The VUV laser pulse of frequency near 123 nm may optionally be triggered on the zero crossing of the RF drive at frequency Ω such that the ions are excited under the same electric field conditions in the trap. This may be important for studying the effects on the Rydberg electron wave packet in the time-dependent potential, theoretically studied in section 4.5. The entire scheme allows for a near 100% discrimination of individual single Rydberg excitation events within a few ms and provides a spatial resolution of the diffraction-limited image of about $2\ \mu\text{m}$, much better than the inter-ion distances, such that we can determine the location and also the correlations of

excitations in the ion crystal. At the end of the sequence, a final optical pumping step (vi) with laser light at 854, 866 and 397 nm brings ions in the whole crystal back to the $S_{1/2}$ ground state. This entire sequence will take about 5–10 ms and will be repeated as the laser frequency ν_{Rydberg} is tuned over the relevant frequency range of the Rydberg levels. Similarly, one may vary the pulse length or apply Ramsey pulses in the Rydberg excitation step.

Let us discuss the differences between the proposed single-photon excitation and a multi-photon excitation process. Firstly, in the case of a multi-photon process driven with high laser powers and high Rabi frequencies there would be a much higher probability to excite ions into the continuum than with a single photon with the relatively low power level. Therefore processes that would lead to double ionization are more easily avoided in our scheme. The advantage of single photon excitation is that a second absorption process from the already excited Rydberg state is very unlikely owing to the relatively low power and the very low probability of this process. In a multi-photon process, however, there are, in general, many more paths for double ionization and one also has to take into account that much higher laser intensities would be used. When the excitation light is generated in the FWM process in Hg vapor, the fundamental wavelengths are separated and do not lead to unwanted ionization. Secondly, the phase relationships in a multi-photon process have to be kept stable, perhaps by using phase locks and an optical comb generator. In addition to the obvious problems from laser phase fluctuations, one may expect large ac Stark shifts from off-resonantly driven dipole transitions [67].

4. Single ion theory

This section is dedicated to a thorough theoretical investigation of the dynamics of a single trapped $^{40}\text{Ca}^+$ ion. We will derive the underlying Hamiltonian, investigate the energy level structure of highly excited Rydberg states and provide a detailed account of the coupled electron–ion dynamics. In the present study, we will particularly focus on Rydberg nP_j states that are laser excited from the metastable $3D_{5/2}$ state. We estimate the dipole-matrix element for this transition and calculate expected shifts of the trap frequency of the ion when excited to Rydberg states. Finally, we analyze possible state changing transitions that occur due to the inevitable coupling of internal and external dynamics of the ion. Simple scaling laws of the above-mentioned effects with respect to the principal quantum number n will be derived.

4.1. Rydberg ion in a linear Paul trap

Here we consider a $^{40}\text{Ca}^+$ ion trapped in a linear Paul trap. The Hamiltonian governing the dynamics of the valence electron and the ionic core can be approximated by the two-body Hamiltonian

$$H = \frac{\mathbf{P}_I^2}{2M} + \frac{\mathbf{p}_e^2}{2m_e} + V(|\mathbf{r}_e - \mathbf{R}_I|) + V_{ls}(\mathbf{r}_e - \mathbf{R}_I) + 2e\Phi(\mathbf{R}_I, t) - e\Phi(\mathbf{r}_e, t), \quad (3)$$

where \mathbf{P}_I (\mathbf{p}_e) and M (m_e) are the momentum and mass of the ion (the electron) and e is the electronic charge. \mathbf{R}_I (\mathbf{r}_e) is the coordinate of the ion (the electron) and the potential $V(|\mathbf{r}_e - \mathbf{R}_I|)$ is an angular-momentum-dependent model potential, which we will discuss in more detail in a subsequent subsection. We consider furthermore the spin–orbit coupling that is accounted for by the operator

$$V_{ls}(\mathbf{r}_e - \mathbf{R}_I) = \frac{\alpha_{ls}^2 \mathbf{l} \cdot \mathbf{s}}{2|\mathbf{r}_e - \mathbf{R}_I|} \frac{dV(|\mathbf{r}_e - \mathbf{R}_I|)}{d(|\mathbf{r}_e - \mathbf{R}_I|)} \quad (4)$$

with $\alpha_{ls} \approx 1/137$ being the fine structure constant. Here \mathbf{l} and \mathbf{s} are the orbital angular momentum and the spin operator of electron, respectively. The last two terms of Hamiltonian (3) emerge from the coupling of the charges to the electric potential of the linear Paul trap. This potential is composed of a static and an RF component reading

$$\Phi(\mathbf{r}, t) = \alpha \cos \Omega t (x^2 - y^2) - \beta(x^2 + y^2 - 2z^2). \quad (5)$$

Here α and β are the electric field gradients of the RF and the static field, respectively, and Ω is the corresponding RF. The combination of these two fields permits the confinement of positively charged particles in the trap center, where they are trapped at the minimum (zero) of an inhomogeneous electric quadrupole field.

It is convenient to treat the system in the center-of-mass frame, in which Hamiltonian (3) becomes

$$H = H_I + H_e + H_{Ie}. \quad (6)$$

Here H_I , H_e and H_{Ie} are the free Hamiltonian of the ion, the Hamiltonian of the electron including electron–trap coupling and the coupling between the electron and the ion, respectively. All of them are explicitly written as

$$H_I = \frac{\mathbf{P}^2}{2M} + e\Phi(\mathbf{R}, t), \quad (7)$$

$$H_e = \frac{\mathbf{p}^2}{2m_e} + V(|\mathbf{r}|) + V_{ls}(\mathbf{r}) - e\Phi(\mathbf{r}, t), \quad (8)$$

$$H_{Ie} = -2e[\alpha \cos \Omega t (Xx - Yy) - \beta(Xx + Yy - 2Zz)], \quad (9)$$

where corrections due to the finite nuclear mass are neglected. The electron–ion coupling H_{Ie} results in an additional potential for the ion. Our calculation shows that for energetically low-lying states, roughly $n < 10$ (see section 4.6), this additional potential is much smaller than the effective trapping potential and thus can be neglected. The static field in conjunction with the rapidly oscillating RF field then gives rise to an effectively static (ponderomotive) harmonic potential for the $^{40}\text{Ca}^+$ ion [68] and the corresponding Hamiltonian of the external motion can be approximated by

$$H_I^{\text{eff}} = \frac{\mathbf{P}^2}{2M} + \frac{M}{2} \sum_{\rho=X,Y,Z} \omega_\rho^2 \rho^2. \quad (10)$$

Here $\omega_r = \omega_x = \omega_y = \sqrt{2[(e\alpha/M\Omega)^2 - e\beta/M]}$ and $\omega_z = 2\sqrt{e\beta/M}$ are the transverse and longitudinal trap frequencies, respectively. Using the trap parameters $\alpha = 1.0 \times 10^9 \text{ V m}^{-2}$, $\beta = 1.0 \times 10^7 \text{ V m}^{-2}$ and $\Omega = 2\pi \times 25 \text{ MHz}$, one obtains $\omega_r = 2\pi \times 3.27 \text{ MHz}$ and $\omega_z = 2\pi \times 1.56 \text{ MHz}$. These values will be used throughout the theory part. They are slightly higher than the ones discussed in section 2 and will make the influence of the trap on the electronic dynamics more prominent. As mentioned before, neglecting the electronic structure when considering the trapping is only valid for low-lying electronic states in which the $^{40}\text{Ca}^+$ ion can be regarded as a singly charged point-like particle. In the Rydberg states in which we are interested here, the spatial extension of the electronic wavefunction can easily become larger than the oscillator length of the trapped ion. To accurately describe ionic Rydberg states, one thus has to account for the coupled electronic and external dynamics.

Our strategy for doing this is to first solve the electronic Hamiltonian excluding the electric trapping potential. This is achieved by diagonalizing the electronic model potential [69], which yields accurate eigenenergies and corresponding wave functions. These states will then constitute a basis in which we can expand the ion–electron coupling. The problem of finding the eigenstates and eigenenergies as well as the time evolution of the system is then reduced to the solution of coupled matrix equations.

4.2. Calculation of Rydberg energies and wave functions

We will now outline the calculation of the field-free electronic wave functions. In this section, we use atomic units throughout unless stated otherwise. The single electron in the outer shell of the $^{40}\text{Ca}^+$ ion moves in the Coulomb potential of the nucleus that is screened by the inner electron shells. In general, this is a complicated many-electron system but since the inner electrons are forming a closed shell it is possible to approximately reduce it to a two-body problem. Here the valence electron is orbiting in an angular-momentum-dependent (i.e. dependent on the quantum number l) model potential that approximates the interaction with the nucleus and the inner shell electrons. Such potential can be parameterized as [69]

$$V_l(r) = -\frac{1}{r}[2 + (Z - 2) \exp(-\alpha_{l,1}r) + \alpha_{l,2}r \exp(-\alpha_{l,3}r)] - \frac{\alpha_{cp}}{2r^4}\{1 - \exp[-(r/r_l)^6]\}, \quad (11)$$

where Z is the nuclear charge, $\alpha_{l,i}$ and r_l are parameters depending on angular momentum and α_{cp} is the experimental dipole polarizability of the doubly charged ion. All these quantities were tabulated in [69]. The spin–orbit interaction is then described by the Hamiltonian

$$V_{l,s}^{(so)}(r) = \frac{\alpha_{ls}^2 \mathbf{l} \cdot \mathbf{s}}{2r} \frac{dV_l(r)}{dr} \left[1 - \frac{\alpha_{ls}^2}{2} V_l(r) \right]^{-2}, \quad (12)$$

where the last factor is introduced to regularize the wave function at the coordinate origin. The model potential conserves the total angular momentum $\mathbf{j} = \mathbf{l} + \mathbf{s}$, which permits an expansion of the electronic wave function into the spinor basis [70]

$$|\psi_{ljm_j}\rangle = \frac{\phi_{l,j}(r)}{r} |l, j, m_j\rangle, \quad (13)$$

where $\phi_{l,j}(r)$ is the radial wave function and $|l, j, m_j\rangle$ denotes the two-component spinor basis vector

$$|ljm_j\rangle = \sum_{m_s=\pm 1/2} \langle l, 1/2, m_l, m_s | j, m_j \rangle |l, m_l\rangle |s s_z\rangle. \quad (14)$$

Here $\langle l, 1/2, m_l, m_j - m_l | j, m_j \rangle$ are the Clebsch–Gordan coefficients and m_j (m_l) is the quantum number of the projection of the angular momentum j (l) onto the quantization axis. Substituting equation (13) into the corresponding Hamiltonian and integrating over the angular variables, we obtain the radial Schrödinger equation

$$\bar{h}_{l,j} \phi_{l,j}(r) = \varepsilon_{l,j} \phi_{l,j}(r), \quad \phi_{l,j}(0) = 0, \quad (15)$$

with the radial Hamiltonian

$$\bar{h}_{l,j} = -\frac{1}{2} \frac{d^2}{dr^2} + \frac{l(l+1)}{2r^2} + V_l(r) + V_{l,s}^{(so)}(r). \quad (16)$$

We solve this equation by discretizing space and diagonalizing the corresponding matrix. The electronic energies obtained from this calculation are in good agreement with the experimental

ones [71]. Hence, we can be confident that the obtained electronic wave functions form a solid foundation for the upcoming analysis of the Rydberg states of the trapped ion.

4.3. Bare electronic level structure

Before treating the coupled electron–ion problem, we will first discuss the energies of the bare electronic states obtained from solving the eigenvalue problem of the radial Hamiltonian (16). We will focus on Rydberg P-states as they are most relevant to the envisioned experimental excitation procedure. The Rydberg P-states of $^{40}\text{Ca}^+$ are split into two manifolds with total angular momentum $j = 1/2$ and $j = 3/2$. Due to the quantum defect these states are furthermore energetically well isolated from adjacent levels. According to Bethe and Salpeter [72], one can parameterize the Rydberg energy, including spin–orbit coupling, according to

$$E_{nlj} = -\frac{Z_c^2}{2(n - \delta_{lj})^2} \left[1 + \frac{(\alpha_{ls} Z_c)^2}{(n - \delta_{lj})} \left(\frac{1}{j + 1/2} - \frac{3}{4(n - \delta_{lj})} \right) \right]. \quad (17)$$

Here Z_c is the net charge of the ionic residue seen by the valence electron. The second term in brackets gives rise to the fine structure splitting due to the spin–orbit interaction. The quantum defects of the nP_j are found by fitting the data with equation (17), $\delta_{1,1/2} = 1.4396$ and $\delta_{1,3/2} = 1.4358$. We have calculated them with respect to the state $3D_{5/2}$, whose energy can be found in [73] and in the NIST database. The huge energy gap, typically a few PHz (1 PHz corresponds to a laser wavelength of $\lambda_L \approx 299.8$ nm), requires a VUV laser for exciting the transition $3D_{5/2} \rightarrow nP_j$. The energy difference (fine-structure splitting) between $nP_{1/2}$ and $nP_{3/2}$, which is shown in the inset of figure 7, is well approximated by $\Delta E_{nlj} \approx \frac{4}{18769}(n - \delta_{lj})^{-3}$, which neglects differences in the quantum defect for different principal quantum numbers. The fine-structure splitting varies from a few tens to hundreds of GHz when $n < 20$, to a few GHz when $20 \leq n < 50$ and reaches sub-GHz when $n \geq 50$. This has to be taken into account when nP_j -states shall be excited selectively from the states $3D_{5/2}$ as the laser linewidth has to be considerably smaller than the energy gap between $nP_{1/2}$ and $nP_{3/2}$.

It is instructive to compare these energy scales with other energies of the system. We use the parameters of section 4.1, i.e. the RF field has the frequency $\Omega = 2\pi \times 25$ MHz, and the oscillation frequencies of the ion in the effective harmonic trap are $\omega_Z \approx 2\pi \times 1.56$ MHz and $\omega_r \approx 2\pi \times 3.27$ MHz with the parameters provided above. Thus, neither the RF field nor the vibrational motion can couple the $P_{1/2}$ to the $P_{3/2}$ manifold resonantly if n is not too large, i.e. $\Delta E_{nlj} \gg \Omega \gg \omega_r \sim \omega_Z$.

4.4. Laser excitation of Rydberg states

The Rabi frequency for the envisioned laser excitation of Rydberg states from the state $3D_{5/2}$ is determined by the dipole-matrix element $\langle 3D_{5/2} | \mathbf{r} | nP_{3/2} \rangle$. In order to obtain an estimate for this matrix element, we calculate the radial wave function of the $3D_{5/2}$ with the model potential (11). We find, for principal quantum numbers > 18 , that

$$\langle 3D_{5/2}(3/2) | z | nP_{3/2}(3/2) \rangle \approx 0.383 \times a_0 n^{-1.588}, \quad (18)$$

with a_0 being Bohr's radius. To estimate the expected Rabi frequency, we use the laser power estimates given in section 3.3. A beam waist of $1.5 \mu\text{m}$ and a laser power of $9 \mu\text{W}$ ($n = 24$) and $27 \mu\text{W}$ ($n = 67$) lead to a Rabi frequency of $2\pi \times 5.2$ MHz ($n = 24$) and $2\pi \times 1.8$ MHz

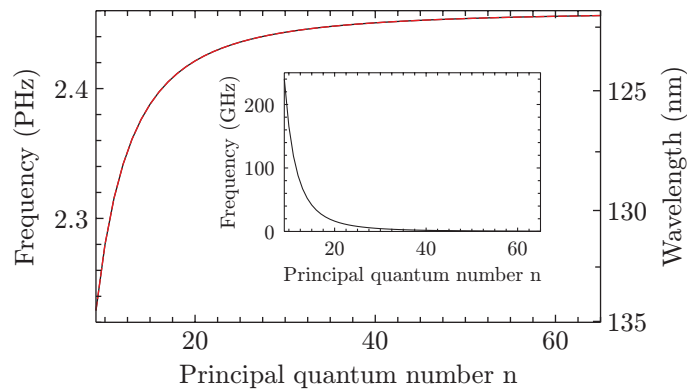


Figure 7. Bare electronic energies of the nP_j Rydberg states. The energy of the states $P_{1/2}$ and $P_{3/2}$ in the field-free case is measured with respect to the state $3D_{5/2}$ as a function of the principal quantum number n . The inset shows the fine-structure splitting between $nP_{1/2}$ and $nP_{3/2}$. Note the different energy units of the inset.

($n = 67$), respectively, when the ion is placed in the laser focus. We have to point out that the present calculation of the $3D_{5/2}$ wave function does not fully take into account correlations of the inner electrons and the valence electron. Hence, the presented value can only be seen as a first estimate and a more rigorous calculation will be needed for more accurate results. On the one hand, the numerically obtained energy of $3D_{5/2}$ agrees well (within 0.04%) with the experimental value given in [71]. On the other, we find significant deviations (up to 8%) when comparing numerically calculated oscillator strengths with experimental values tabulated in [74].

This concludes our discussion of the level structure of $^{40}\text{Ca}^+$ in the field-free case. Before turning to the discussion of the coupled electronic and ionic dynamics, we will investigate in the following two subsections the electron–trap and the electron–ion interaction in order to gain a better understanding of the system.

4.5. Electron–trap interaction

To calculate the interaction of the valence electron with the electric fields of the Paul trap, one has, in principle, to expand the entire Hamiltonian (6) in the electronic basis and then subsequently diagonalize it or propagate the desired initial wave function. This is particularly difficult when dealing with Rydberg states due to a high density of states which will lead to a high-dimensional matrix. To circumvent this problem we exploit—as earlier mentioned—that the nP -manifold is well isolated from other states. This permits the derivation of an effective Hamiltonian that acts only in this low-dimensional electronic subspace but takes into account the couplings to other electronic states perturbatively. The derivation of this Hamiltonian is based on the van Vleck transformation [75]. This procedure greatly reduces the dimension of the matrices involved and therefore simplifies the calculation and analysis of the problem considerably. The effective electronic Hamiltonian becomes six dimensional.

We now turn to the calculation of the electronic level shifts due to the electron–trap interaction in equation (8). The interaction Hamiltonian can be written explicitly in the spherical

coordinates and reads

$$H_{\text{et}} = -4\sqrt{\frac{\pi}{5}}e\beta r^2 Y_2^0(\theta, \phi) - 2\sqrt{\frac{2\pi}{15}}e\alpha r^2 \cos \Omega t [Y_2^2(\theta, \phi) + Y_2^{-2}(\theta, \phi)]. \quad (19)$$

This means that we are actually calculating the electronic level shift for a situation in which the ion is located perfectly at the trap center. In this subsection, we consider the time t merely as a parameter. This quasi-static approximation seems reasonable since the frequency of the RF field is typically much smaller than the frequency associated with the motion of the Rydberg electron. At a later stage we will, however, take full account of the time dependence when describing the coupled electron–ion dynamics.

As indicated in the introductory paragraph of this section, the level shifts caused by H_{et} are much smaller than the distance between the field-free electronic eigenenergies E_{nlj} . We can thus calculate them by using second-order perturbation theory. The corresponding van Vleck transformation yields the following effective interaction Hamiltonian in the reduced nP_j -subspace:

$$H_{\text{et}}^{(2)mm'} = \sum_{\nu} H_{\text{et}}^{(1)m\nu} H_{\text{et}}^{(1)\nu m'} \left[\frac{1}{2(E_m - E_{\nu})} + \frac{1}{2(E_{m'} - E_{\nu})} \right]. \quad (20)$$

Here the sum over $\nu = \{n, l, j, m_j\}$ excludes all states in the nP_j -subspace of interest and $H_{\text{et}}^{(1)m\nu} = \langle \psi_m | H_{\text{et}} | \psi_{\nu} \rangle$. From the selection rules imposed by the structure of equation (19) (the orbital angular momentum of two coupled states has to differ by ± 2), it is evident that the matrix elements $H_{\text{et}}^{(1)m\nu}$ will not couple any electronic state within the nP_j subspace directly. The coupling, however, can happen indirectly through intermediate states as shown by equation (20). Here our numerical calculations show that the diagonal matrix elements of equation (20) are always larger than the off-diagonal elements at any moment. For example, at $\alpha = 10^9 \text{ V m}^{-2}$ and $\beta = 10^7 \text{ V m}^{-2}$, the ratio of the diagonal elements to the off-diagonal elements of the state 35P varies in the range 4–200. Therefore, the electronic level shifts are mostly determined by these diagonal entries.

The numerical results for the diagonal matrix elements, as functions of the electric field gradients α and β for the manifold 35P, are depicted in figure 8. When $\Omega t = \pi/2$, the terms involving α actually vanish. Here the energy shifts $H_{\text{et}}^{(2)mm'}$ are determined solely by β , i.e. the static electric field of the trap. For the range of principal quantum numbers shown, the variation of β causes a shift of the electronic energies which is of the order of a few hundreds of kHz. However, since usually $\alpha \gg \beta$ the RF field is causing much stronger level shifts, which for the data shown can be up to a few MHz when $|\cos(\Omega t)| = 1$. This time dependence of the electronic energies has to be accounted for when the Rydberg states of a trapped ion are laser excited from low-lying states.

For all times, one finds that the states of the 35P manifold are shifted to a lower energy compared to the bare electronic states, due to the level repulsion from states above nP_j . Hence the electric field mostly causes mixing of nP_j with the nearby manifold of F -states. The energy shifts $H_{\text{et}}^{(2)mm'}$ depend rather sensitively on the principal quantum number n . From equations (19) and (20) one finds that they scale according to n^{11} , due to $\langle r^2 \rangle \sim n^4$ and $\Delta E_{nlj} \sim n^{-3}$. In figure 8, we show numerical results (for $|\cos \Omega t| = 1$) that indeed confirm the scaling. Energy shifts of up to several hundreds of MHz can be found when $n > 60$. To treat these high-lying states accurately, however, requires one to go beyond the second order in the perturbation expansion. Moreover, such high principal quantum numbers necessitate the consideration of field ionization, a discussion of which can be found in [24].

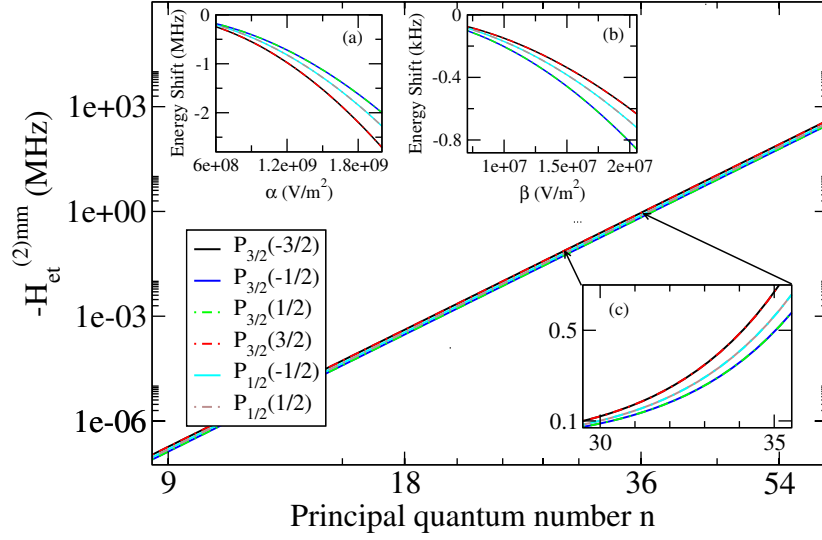


Figure 8. Electron–trap interaction under the assumption of a quasi-static RF field. Here we plot the diagonal electronic energy shift $H_{\text{et}}^{(2)mm}$ as a function of the principal quantum number n for $\Omega t = k\pi$ with integer k (log–log scale). (a, b) Dependence of the electron–trap interaction on α and β at different times t . (a) $\Omega t = k\pi$; here the RF field reaches its maximal amplitude and causes the strongest level shifts. (b) $\Omega t = k\pi + \pi/2$; here terms involving α vanish and only the static field component of the Pauli trap (with magnitude β) determines the energy shifts. (c) Magnification of the energy shifts in the region $n = 30$ – 35 . In (c), linear scale is used. The parameters for which the data are calculated are $\Omega = 2\pi \times 25$ MHz, $\alpha = 10^9$ V m $^{-2}$ and $\beta = 10^7$ V m $^{-2}$.

4.6. Electron–ion coupling

We will now focus on the actual electron–ion interaction which is effectuated by the inhomogeneous nature of the electric fields forming the Pauli trap. Similar couplings are also observed in the context of Rydberg atoms that are trapped by means of inhomogeneous magnetic fields [76, 77]. For trapped ions the corresponding coupling Hamiltonian is H_{Ie} (equation (9)).

To treat it, we will again make use of the van Vleck transformation which yields the following matrix elements of the effective coupling Hamiltonian in the nP_j -subspace:

$$H_{\text{Ie}}^{(2)mm'} = \mathbf{R}^\dagger \mathbf{U}_{mm'} \mathbf{R}, \quad (21)$$

where \mathbf{R} is the position of the ion and

$$\mathbf{U}_{mm'} = \sum_{\nu} \mathbf{R}_e^{\dagger(1)mv} \mathbf{R}_e^{(1)\nu m'} \left[\frac{1}{2(E_m - E_\nu)} + \frac{1}{2(E_{m'} - E_\nu)} \right]. \quad (22)$$

Here we have used the abbreviations $\mathbf{R}_e^{(1)mv} = \langle \psi_m | \mathbf{R}_e | \psi_\nu \rangle$ and $\mathbf{R}_e = 2e[(-\alpha \cos \Omega t + \beta)x, (\alpha \cos \Omega t + \beta)y, -2\beta z]$. When the electron is in the low-lying states the energy shifts caused by equation (21) are negligible in comparison to the typical spacing between vibrational energies of the ion. This is due to the fact that the coupling is roughly proportional to the size of the electronic orbit because it depends on the relative coordinate \mathbf{r} of the ion–electron system.

The situation is changed when the electron is excited to Rydberg states. Here the large orbit of the electron, $\langle r \rangle \sim a_0 n^2$, leads to a substantial change of the magnitude of equation (21).

The coupling caused by equation (21) can affect the motion of the ion in two possible ways: firstly, the effective time-averaged potential that governs the external ionic motion is not separable anymore, because the off-diagonal matrix elements of $U_{mm'}$ couple the ionic vibrations in different directions. Secondly, the diagonal elements of $U_{mm'}$ will lead to an additional trapping potential for the ion that is superimposed on the already present harmonic confinement.

To quantify the strength of the additional trapping potential that is effectuated by the electron–ion coupling, we calculate the time-averaged energy shift ΔE_X^{mm} of the electronic energy as a function of the displacement in the X -direction from the coordinate center. Using equation (21), the result is

$$\Delta E_X^{mm} \approx e^2 (2\alpha^2 + 4\beta^2) \mathcal{V}_{\text{Ie}}^{(2)mm} X^2, \quad (23)$$

where $\mathcal{V}_{\text{Ie}}^{(2)mm}$ is a parameter that depends only on the electronic states. It scales as $\sim n^7$. The harmonic frequency of this additional potential can be estimated in accordance with equation (23) to yield

$$\Delta\omega_X = \sqrt{\frac{2e^2(2\alpha^2 + 4\beta^2)\mathcal{V}_{\text{Ie}}^{(2)mm}}{M}}. \quad (24)$$

This result does not take into account modifications of the trap frequency that arise from cross-couplings to the oscillatory motion in the Y - and Z -directions and is thus merely an estimate.

Note that $\Delta\omega_X \sim \sqrt{\alpha^2 + 2\beta^2} \sim \alpha$ and $\Delta\omega_X \sim \sqrt{\mathcal{V}_{\text{Ie}}^{(2)mm}} \sim n^{7/2}$. This scaling indicates that the oscillation frequencies of a trapped ion can be substantially modified when the electron is excited to Rydberg states. In figure 9, we show some numerical results obtained for $^{40}\text{Ca}^+$. One observes that for very-high-lying Rydberg states the trap frequency $\Delta\omega_X$ of the additional potential becomes even comparable to ω_X itself. This indicates that a description of the external ionic motion through harmonic oscillators might break down entirely.

4.7. Adiabatic potential surfaces

In the previous two sections, the individual electron–trap and electron–ion interactions were investigated. This analysis provided us with basic insights into the coupled ion–electron dynamics. We are now in a position to study the complete interaction Hamiltonian in equations (8) and (9). Such treatment poses difficulties, in particular when dealing with the oscillating RF field. The conventional approximations usually made in the case of such oscillating fields, e.g. the rotating wave approximation, are hard to carry out in the present problem, as quite a few different time scales are involved (see section 4.3).

To make progress we employ once again the approximation of a quasi-static electric field that has already been used in section 4.5, i.e. we calculate the eigenvalues of the sum of Hamiltonians (8) and (9) while taking time as a parameter. As a result we obtain four-dimensional (three spatial and one temporal axes) adiabatic potential surfaces. In figure 10, we show a cut (along X and Ωt) through the surfaces that belong to the states $35\text{P}_{3/2}$. We do not show the contribution of the ionic center-of-mass Hamiltonian (7), which just gives rise to a state-independent potential.

We observe two pairs of degenerate potential surfaces. This degeneracy is typical for Hamiltonians representing half-inter-spin particles and a time-reversal invariant Hamiltonian. It

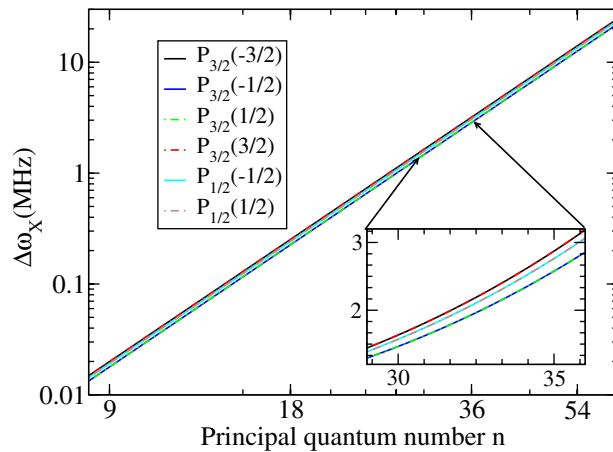


Figure 9. Estimated trap frequency $\Delta\omega_X$ of the additional potential induced by the electron–ion coupling in Rydberg states. The dependence of $\Delta\omega_X$ on the principal quantum number n is shown (log–log scale). The curves shown scale according to $\sim n^{7/2}$. Here $\Omega = 2\pi \times 25$ MHz, $\alpha = 10^9$ V m $^{-2}$ and $\beta = 10^7$ V m $^{-2}$.

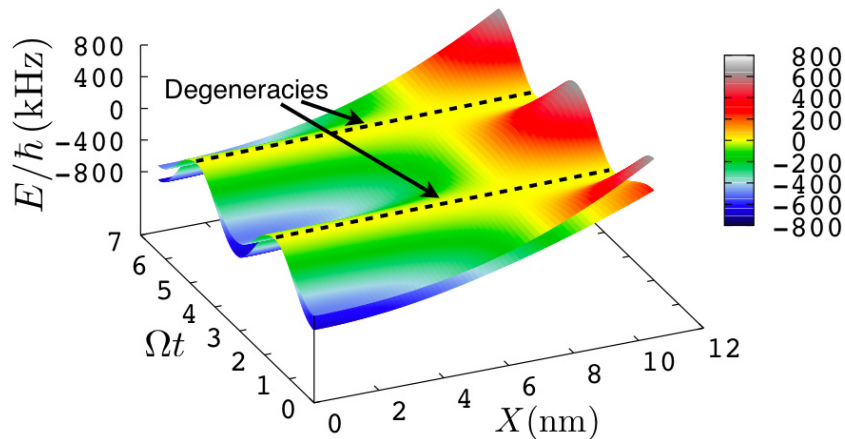


Figure 10. Adiabatic potential surface of the $35P_{3/2}$. The potential surface is plotted along the X – Ωt -plane. The dashed curves are lines along which degeneracies occur. Here $\Omega = 2\pi \times 25$ MHz, $\alpha = 10^9$ V m $^{-2}$ and $\beta = 10^7$ V m $^{-2}$.

is called Kramer’s degeneracy [78]. In addition, all four potential surfaces become completely degenerate (in the X – Ωt -plane) when $\cos \Omega t = \beta/\alpha$. Note that complete degeneracy can occur only in the X – Y -plane at particular moments in time, namely when the static and RF fields cancel. These degeneracies induce nonadiabatic transitions between neighboring electronic states, which forbid the application of a single-surface Born–Oppenheimer approximation for the description of the coupled ion–electron system. One thus has to solve the complete quantum problem consisting of the three external ionic degrees of freedom plus the six-dimensional electronic state space of the nP_j -manifold.

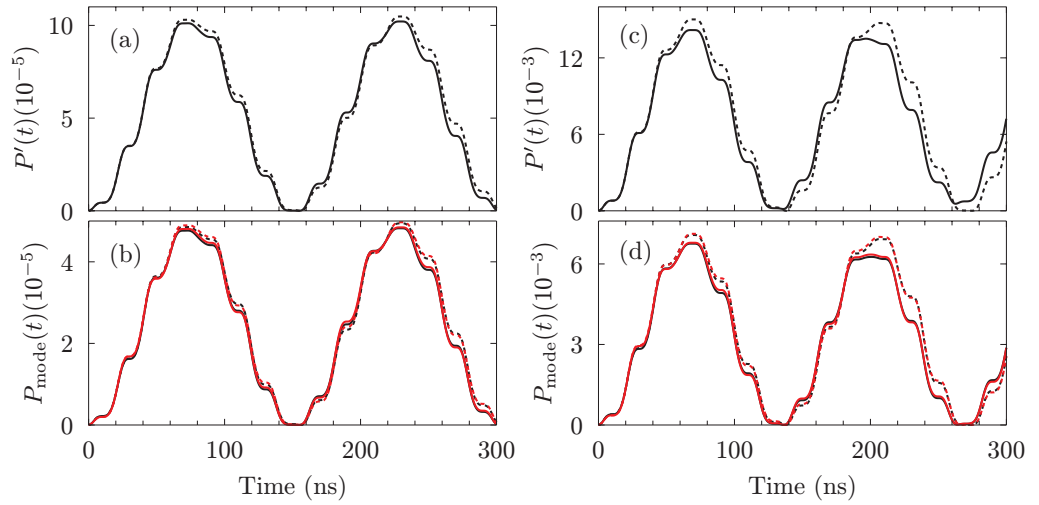


Figure 11. Population dynamics. (a, b) The initial electronic state is $|35P_{3/2}(3/2)\rangle$. (a) Population loss from the initial state $|000\rangle|35P_{3/2}(3/2)\rangle$. (b) In the course of the time evolution, population is transferred to the states $|200\rangle|35P_{3/2}(3/2)\rangle$ (red) and $|020\rangle|35P_{3/2}(3/2)\rangle$ (black). The electronic state is virtually unchanged. (c, d) The initial electronic state is $|50P_{3/2}(3/2)\rangle$. (c) Population loss from the initial state $|000\rangle|50P_{3/2}(3/2)\rangle$. (d) The time evolution of dominant modes $|200\rangle|50P_{3/2}(3/2)\rangle$ (red) and $|020\rangle|50P_{3/2}(3/2)\rangle$ (black). During the time interval shown, there is no significant transition to the states $nP_{j \neq j_0}$. In all the panels, solid/dashed curves correspond to numerical simulation/time-dependent perturbation theory. The parameters used in the simulation are $\Omega = 2\pi \times 25$ MHz, $\alpha = 10^9$ V m $^{-2}$ and $\beta = 10^7$ V m $^{-2}$.

4.8. State-changing transitions in the nP_j -manifold

The degeneracies shown in figure 10 can in principle lead to nonadiabatic transitions among the electronic states of the nP_j -manifold. Such state-changing transitions are certainly not desirable, in particular when ionic Rydberg states are excited for the purpose of implementing quantum information processing protocols. We will now study the severity of this effect in more detail by analyzing the temporal evolution of a wave packet in which the ion is initially prepared in the state

$$|\Psi(0)\rangle = |000\rangle|35P_{3/2}(3/2)\rangle, \quad (25)$$

where $|000\rangle$ is the ground state of the effective harmonic oscillator Hamiltonian (10) (to characterize the vibrational state we use the notation $|n_x n_y n_z\rangle$, where n_k corresponds to the number of vibrational quanta in the k th direction). The state $|\Psi(0)\rangle$ can be approximately created by a fast π -pulse on the transition $3D_{5/2}(5/2) \rightarrow 35P_{3/2}(3/2)$ applied to an ion that is cooled to the external ground state. We will study the evolution under the action of the Hamiltonian (6) where we replace H_I by the effective Hamiltonian (10). This approach neglects the micromotion. We are interested in the population of states other than $|\Psi(0)\rangle$ as a function of time.

In figure 11, we show the corresponding plot calculated for the parameters $\Omega = 2\pi \times 25$ MHz, $\alpha = 10^9$ V m $^{-2}$ and $\beta = 10^7$ V m $^{-2}$. The time interval shown corresponds to twice the

period of the transverse external ionic motion $4\pi/\omega_r$. Apart from the numerically exact result, we also present the loss of population calculated from time-dependent perturbation theory. Both curves are in excellent agreement, showing only a marginal ‘loss’ of population from the initial state which oscillates periodically at a frequency of about $2\pi \times 6.7$ MHz. The maximum loss, which is about 0.01%, is reached at about 70 ns. The fast oscillations visible on top of the curve are due to the RF field. The absence of loss for this particular set of parameters is partially because all the transition matrix elements are small. For instance, the maximal off-diagonal matrix elements of the electron–ion interaction are here about $2\pi \times 400$ kHz, which is several times smaller than the diagonal matrix elements in equation (21). Moreover, the RF field is far off-resonant with all the transition energies, as shown in section 4.3.

A further analysis of the wave packet propagation shows that essentially only the states $|200\rangle|35P_{3/2}(3/2)\rangle$ and $|020\rangle|35P_{3/2}(3/2)\rangle$ are populated in the course of the time evolution. The corresponding data are presented in figure 11(b). This demonstrates that virtually no transitions among electronic states are taking place and that solely the population of the external trap levels is slightly redistributed.

Although population transfer is small for the state $|35P_{3/2}\rangle$, it can become significant for higher Rydberg states. The matrix elements for transitions between vibrational modes are proportional to $U_{mm'}$ and scale in proportion to n^7 . As a result, the maximal population of the excited states can be estimated to be proportional to n^{14} as long as perturbation theory applies. As an example, we calculated the loss dynamics for the state $|50P_{3/2}(3/2)\rangle$. The corresponding data are shown in figures 11(c) and (d). The fully numerical calculations show that the loss of the population from the initial state is about 143 times larger than that from the state $|35P_{3/2}(3/2)\rangle$, which is in good agreement with the scaling. Moreover, at higher Rydberg states the dramatic increase of the transition matrix elements and the effective trap frequency gives rise to higher oscillation frequencies, which is clearly shown in the dynamics of the dominant modes, also depicted in figures 11(c) and (d). Consequently, the redistribution of the population of the external modes becomes more important at the higher Rydberg states.

5. Conclusion and outlook

So far our study revealed no conceptual obstacles that speak against the feasibility of coherently exciting Rydberg states of trapped $^{40}\text{Ca}^+$ ions. The calculation of the spectral data presented in this work relies heavily on the accuracy of the model potential that was used to calculate the Rydberg wave functions [69]. First experiments will thus allow us to assess the accuracy of these data. These results will be fed back into the calculations for further improvement and refinement of the theoretical predictions. Most importantly, experiments will measure accurately the transition frequencies and the dipole matrix element for the transition $3D_{5/2} \rightarrow nP_{3/2}$ for which we could only provide an estimate in section 4.4.

This, together with accurate spectroscopic data, will direct the next step in which we intend to carry out a detailed study of the interaction properties between ionic Rydberg states. As in the single ion case, the consequences of the coupling between the internal and the external ion dynamics caused by the inhomogeneous trapping field will have to be understood. We expect that, unlike in the case of neutral atoms, the van der Waals interaction among excited ions will be too weak to achieve large (of the order of MHz) interaction energies. To overcome this problem we intend to study the possibility to ‘dress’ Rydberg with microwave photons. In [24], it was shown that this is a promising route towards strongly interacting spin models and fast quantum

gates. Quantum state tomography and quantum process tomography have been well established when using the low-lying qubit states $S_{1/2}$ and $D_{5/2}$ in $^{40}\text{Ca}^+$. This technique will allow us to characterize the entanglement operations by the Rydberg excitation. In the longer run, one might address single ions with the tightly focused VUV beams in the setting indicated by figure 1(b), analogous to the experiments with neutral atoms trapped in focused laser beams [7, 8].

Beyond that, the envisioned experimental setup might be potentially used to study novel hybrid quantum states in ion traps, where one highly excited electron is shared among two or more core ions [79]. This would pave the way for an entirely new regime in trapped ion physics. Finally, Rydberg states of ions could be coupled to microwave resonators and strip line cavities, as discussed for atoms in [80], but now as hybrid solid state–trapped ion systems in the spirit of Tian *et al* [81].

Acknowledgments

IL acknowledges funding from EPSRC. WL acknowledges funding through a Marie Curie Fellowship from the European Union. MM and PZ acknowledge support from the Austrian Science Fund (FOQUS), the European Commission (AQUITE) and the Institute of Quantum Information. The authors represent the R-ION consortium funded by the EU through the CHIST-ERA call.

References

- [1] Saffman M, Walker T G and Mølmer K 2010 *Rev. Mod. Phys.* **82** 2313
- [2] Jaksch D, Cirac J I, Zoller P, Rolston S L, Côté R and Lukin M D 2000 *Phys. Rev. Lett.* **85** 2208
- [3] Lukin M D, Fleischhauer M, Cote R, Duan L M, Jaksch D, Cirac J I and Zoller P 2001 *Phys. Rev. Lett.* **87** 037901
- [4] Beige A, Huelga S, Knight P, Plenio M B and Thompson R C 2000 *J. Mod. Opt.* **47** 401
- [5] Singer K, Reetz-Lamour M, Amthor T, Marcassa L G and Weidemüller M 2004 *Phys. Rev. Lett.* **93** 163001
- [6] Heidemann R, Raitzsch U, Bendkowsky V, Butscher B, Löw R, Santos L and Pfau T 2007 *Phys. Rev. Lett.* **99** 163601
- [7] Gaëtan A, Miroshnychenko Y, Wilk T, Chotia A, Viteau M, Comparat D, Pillet P, Browaeys A and Grangier P 2009 *Nat. Phys.* **5** 115
- [8] Urban E, Johnson T A, Henage T, Isenhower L, Yavuz D D, Walker T G and Saffman M 2009 *Nat. Phys.* **5** 110
- [9] Isenhower L, Urban E, Zhang X L, Gill A T, Henage T, Johnson T A, Walker T G and Saffman M 2010 *Phys. Rev. Lett.* **104** 010503
- [10] Wilk T, Gaëtan A, Evellin C, Wolters J, Miroshnychenko Y, Grangier P and Browaeys A 2010 *Phys. Rev. Lett.* **104** 010502
- [11] Pupillo G, Micheli A, Boninsegni M, Lesanovsky I and Zoller P 2010 *Phys. Rev. Lett.* **104** 223002
- [12] Henkel N, Nath R and Pohl T 2010 *Phys. Rev. Lett.* **104** 195302
- [13] Weimer H, Löw R, Pfau T and Büchler H P 2008 *Phys. Rev. Lett.* **101** 250601
- [14] Olmos B, Müller M and Lesanovsky I 2010 *New J. Phys.* **12** 013024
- [15] Lesanovsky I, Olmos B and Garrahan J 2010 *Phys. Rev. Lett.* **105** 100603
- [16] Olmos B, González-Férez R and Lesanovsky I 2009 *Phys. Rev. Lett.* **103** 185302
- [17] Pohl T, Demler E and Lukin M D 2010 *Phys. Rev. Lett.* **104** 043002
- [18] Schachenmayer J, Lesanovsky I, Micheli A and Daley A 2010 *New J. Phys.* **12** 103044
- [19] Müller M, Lesanovsky I, Weimer H, Büchler H P and Zoller P 2009 *Phys. Rev. Lett.* **102** 170502

- [20] Lesanovsky I 2011 *Phys. Rev. Lett.* **106** 025301
- [21] Weimer H, Müller M, Lesanovsky I, Zoller P and Büchler H P 2010 *Nat. Phys.* **6** 382–8
- [22] Younge K C, Knuffman B, Anderson S E and Raithel G 2010 *Phys. Rev. Lett.* **104** 173001
- [23] Whitlock S, Gerritsma R, Fernholz T and Spreuw R J C 2009 *New J. Phys.* **11** 023021
- [24] Müller M, Liang L, Lesanovsky I and Zoller P 2008 *New J. Phys.* **10** 093009
- [25] James D 1998 *Appl. Phys. B* **66** 181
- [26] Blatt R and Wineland D J 2008 *Nature* **453** 1008
- [27] Häffner H, Roos C F and Blatt R 2008 *Phys. Rep.* **469** 155
- [28] Nägerl H C, Leibfried D, Rohde H, Thalhammer G, Eschner J, Schmidt-Kaler F and Blatt R 1999 *Phys. Rev. A* **60** 145
- [29] Benhelm J, Kirchmair G, Roos C F and Blatt R 2008 *Nat. Phys.* **4** 463
- [30] Riebe M *et al* 2004 *Nature* **429** 734
- [31] Barrett M D *et al* 2004 *Nature* **429** 839
- [32] Monz T, Schindler P, Barreiro J T, Chwalla M, Nigg D, Coish W A, Harlander M, Hänsel W, Hennrich M and Blatt R 2011 *Phys. Rev. Lett.* **106** 130506
- [33] Porras D and Cirac J I 2004 *Phys. Rev. Lett.* **92** 207901
- [34] Friedenauer A, Schmitz H, Glückert J, Porras D and Schätz T 2008 *Nat. Phys.* **4** 757
- [35] Kim K, Chang M S, Korenblit S, Islam R, Edwards E E, Freericks J K, Lin G D, Duan L M and Monroe C 2010 *Nature* **465** 590
- [36] Müller M, Hammerer K, Zhou Y L, Roos C F and Zoller P 2011 arXiv:1104.2507
- [37] Barreiro J T, Müller M, Schindler P, Nigg D, Monz T, Chwalla M, Hennrich M, Roos C F, Blatt R and Zoller P 2011 *Nature* **470** 486
- [38] Cirac I and Zoller P 1995 *Phys. Rev. Lett.* **74** 4091
- [39] Sorensen A and Molmer K 1999 *Phys. Rev. Lett.* **82** 1971
- [40] Kielpinski D, Monroe C and Wineland D 2002 *Nature* **417** 709
- [41] Home J P, Hanneke D, Jost J D, Amini J M, Leibfried D and Wineland D J 2009 *Science* **325** 1227
- [42] Huber G, Deuschle T, Schnitzler W, Reichle R, Singer K and Schmidt-Kaler F 2008 *New J. Phys.* **10** 013004
- [43] Welzel J, Bautista-Salvador A, Abarbanel C, Wineman-Fisher V, Wunderlich C, Folman R and Schmidt-Kaler F 2011 arXiv:1102.3645
- [44] Schmied R, Wesenberg J H and Leibfried D 2009 *Phys. Rev. Lett.* **102** 233002
- [45] Xu C B, Xie X P, Zhao R C, Sun W, Xue P, Zhong Z P, Huang W and Xu X Y 1998 *J. Phys. B: At. Mol. Opt. Phys.* **31** 5355
- [46] Eikema K S E, Walz J and Hänsch T W 2001 *Phys. Rev. Lett.* **86** 5679
- [47] Scheid M, Kolbe D, Markert F, Hänsch T W and Walz J 2009 *Opt. Express* **17** 11274
- [48] Kolbe D, Koglbauer A, Scheid M and Walz J to be published
- [49] Denison D 1971 *J. Vac. Sci. Tech.* **8** 266
- [50] Leibfried D, Blatt R, Monroe C and Wineland D 2003 *Rev. Mod. Phys.* **75** 281
- [51] Fröhlich U, Roth B and Schiller S 2005 *Phys. Plasmas* **12** 073506
- [52] Enzer D G *et al* 2000 *Phys. Rev. Lett.* **85** 2466–9
- [53] Singer K, Poschinger U, Murphy M, Ivanov P, Ziesel F, Calarco T and Schmidt-Kaler F 2010 *Rev. Mod. Phys.* **82** 2609
- [54] Schulz S A, Poschinger U, Ziesel F and Schmidt-Kaler F 2008 *New J. Phys.* **10** 045007
- [55] Eikema K S E, Walz J and Hänsch T W 1999 *Phys. Rev. Lett.* **83** 3828
- [56] Walz J, Pahl A, Eikema K S E and Hänsch T W 2001 *Nucl. Phys. A* **692** 163
- [57] Pahl A, Fendel P, Henrich B R, Walz J, Hänsch T W and Eikema K S E 2005 *Laser Phys.* **15** 46
- [58] Bjorklund G C 1975 *IEEE J. Quantum Electron.* **11** 287
- [59] Smith A V, Alford W J and Hadley G R 1988 *J. Opt. Soc. Am. B* **5** 1503
- [60] Scheid M, Markert F, Walz J, Wang J, Kirchner M and Hänsch T W 2007 *Opt. Lett.* **32** 955
- [61] Pask H M, Carman R J, Hanna D C, Tropper A C, Mackechnie C J, Barber P R and Dawes J M 1995 *IEEE J. Quantum Electron.* **1** 2

- [62] Paschotta R, Nilsson J, Tropper A C and Hanna D C 1997 *IEEE J. Quantum Electron.* **33** 1049
- [63] Kolbe D, Beczkowiak A, Diehl T, Koglbauer A, Müllers A, Scheid M, Stappel M, Steinborn R and Walz J 2011 *Can. J. Phys.* **89** 25
- [64] Kreuter A *et al* 2005 *Phys. Rev. A* **71** 032504
- [65] Wunderlich C *et al* 2007 *J. Mod. Opt.* **54** 1541
- [66] Djerad M T 1991 *J. Physique II* **1** 1
- [67] Haeffner H, Gulde S, Riebe M, Lancaster G, Becher C, Eschner J, Schmidt-Kaler F and Blatt R 2003 *Phys. Rev. Lett.* **90** 143602
- [68] Cook R J, Shankland D G and Wells A L 1985 *Phys. Rev. A* **31** 564
- [69] Aymar M, Greene C H and Luc-Koenig E 1996 *Rev. Mod. Phys.* **68** 1015
- [70] Friedrich H S 2005 *Theoretical Atomic Physics* 3rd edn (Berlin: Springer)
- [71] Greene C H and Kim L 1987 *Phys. Rev. A* **36** 2706
- [72] Bethe H A and Salpeter E E 2008 *Quantum Mechanics of One- and Two-Electron Atoms* Dover reprint (New York: Dover)
- [73] Safronova M S and Safronova U I 2011 *Phys. Rev. A* **83** 012503
- [74] Theodosiou C E 1989 *Phys. Rev. A* **39** 4880–3
- [75] Shavitt I and Redmon L T 1980 *J. Chem. Phys.* **73** 5711
- [76] Hezel B, Lesanovsky I and Schmelcher P 2006 *Phys. Rev. Lett.* **97** 223001
- [77] Mayle M, Lesanovsky I and Schmelcher P 2009 *Phys. Rev. A* **79** 041403
- [78] Landau L D and Lifshitz L M 1981 *Quantum Mechanics: Non-Relativistic Theory* 3rd edn (New York: Butterworth-Heinemann)
- [79] Lesanovsky I, Müller M and Zoller P 2009 *Phys. Rev. A* **79** 010701
- [80] Sørensen A S, van der Wal C H, Childress L I and Lukin M D 2004 *Phys. Rev. Lett.* **92** 063601
- [81] Tian L, Rabl P, Blatt R and Zoller P 2004 *Phys. Rev. Lett.* **92** 247902